

A multi-material platform for imaging of single cell-cell junctions under tensile load fabricated with two-photon polymerization

Jordan Rosenbohm¹ · Grayson Minnick¹ · Bahareh Tajvidi Safa¹ · Amir Monemian Esfahani¹ · Xiaowei Jin¹ · Haiwei Zhai¹ · Nickolay V. Lavrik² · Ruiguo Yang^{1,3}

Accepted: 4 September 2022 / Published online: 8 October 2022 © The Author(s), under exclusive licence to Springer Science+Business Media, LLC, part of Springer Nature 2022

Abstract

We previously reported a single-cell adhesion micro tensile tester (SCAµTT) fabricated from IP-S photoresin with two-photon polymerization (TPP) for investigating the mechanics of a single cell-cell junction under defined tensile loading. A major limitation of the platform is the autofluorescence of IP-S, the photoresin for TPP fabrication, which significantly increases background signal and makes fluorescent imaging of stretched cells difficult. In this study, we report the design and fabrication of a new SCAµTT platform that mitigates autofluorescence and demonstrate its capability in imaging a single cell pair as its mutual junction is stretched. By employing a two-material design using IP-S and IP-Visio, a photoresin with reduced autofluorescence, we show a significant reduction in autofluorescence of the platform. Further, by integrating apertures onto the substrate with a gold coating, the influence of autofluorescence on imaging is almost completely mitigated. With this new platform, we demonstrate the ability to image a pair of epithelial cells as they are stretched up to 250% strain, allowing us to observe junction rupture and F-actin retraction while simultaneously recording the accumulation of over 800 kPa of stress in the junction. The platform and methodology presented here can potentially enable detailed investigation of the mechanics of and mechanotransduction in cell-cell junctions and improve the design of other TPP platforms in mechanobiology applications.

Keywords Two-photon polymerization · Cell stretch · Fluorescent imaging · Cell-cell junction · Autofluorescence

1 Introduction

The study of mechanical properties of cell-cell junctions has seen increased interest in recent years due to advanced technologies that allow for precise cell manipulation and complex microstructures with fine resolution to interact with cells. For studying cell-cell junction mechanics, two common approaches are dual micropipette aspiration (DPA)

- ⊠ Ruiguo Yang ryang6@unl.edu
- Department of Mechanical and Materials Engineering, University of Nebraska-Lincoln, Lincoln, NE 68588, USA
- ² Center for Nanophase Materials Sciences, Oak Ridge National Laboratory, Oak Ridge, TN 37831-6054, USA
- Nebraska Center for Integrated Biomolecular Communication, University of Nebraska-Lincoln, Lincoln, NE 68588, USA

(Tabdili et al. 2012; Vedula et al. 2009) and single cell force spectroscopy (SCFS) (Friedrichs et al. 2013; Panorchan et al. 2006). In DPA, two cells are suctioned onto the tip of two micropipettes, brought into contact and subsequently pulled apart, while the force within the junction is determined based on the deflection of the micropipette tips. A major limitation of this experimental setup is that cells are not given time to form mature focal adhesions, which play a critical role in adhesion-mediated mechanotransduction (Esfahani et al. 2021). In addition, this platform has difficulty in combining mechanical measurements with fluorescence microscopy (González-Bermúdez et al. 2019). In SCFS, one cell is attached to an atomic force microscopy (AFM) probe and brought into contact with another cell on a petri dish, and then the cells are pulled apart while force is read with the AFM. While this technique allows for a high force sensing resolution, a major limitation is the difficulty in continuously observing the cell-cell junction during stretching due to the orientation of the stretching direction with respect to the imaging plane. In addition, like



with DPA, mature cell-cell junctions cannot form without sacrificing throughput.

To address these limitations, our group designed a singlecell adhesion micro tensile tester (SCAµTT) platform, which allows for stretching a single pair of cells connected by a junction while imaging it and recording stress and strain (Esfahani et al. 2021). In addition, cells are allowed time for prolonged growth on the platform to form mature cell-cell junctions and focal adhesions, and since an array of these platforms are fabricated on one substrate, parallel operation and high throughput is achieved. However, a major limitation of this platform for studying mechanotransduction is the optical properties of IP-S, the photoresin it was originally fabricated with, which produces high autofluorescence during fluorescent imaging. Fluorescent imaging is critical in investigating mechanotransduction, as it allows for real-time visualization of the expression and organization of proteins tagged with fluorescent markers as well as investigation of force-induced protein unfolding with fluorescence resonant energy transfer (FRET). By enabling fluorescent imaging on this platform, a variety of mechanotransduction responses can be further studied. For example, initiation of mechanotransduction responses in both adherens junctions and desmosomes can be studied with FRET sensor incorporated into E-cadherin, α-catenin, and desmoplakin. Further, the dynamics of downstream responses, such as reorganization of F-actin and intermediate filaments, as well as clustering of junctional proteins, can be investigated. Finally, force transmission through the junction and onto cell-ECM junctions can be studied using DNA-based tension sensors and traction force microscopy. The high background signal produced by IP-S makes conducting these types of studies difficult, especially FRET studies, due to its inherently weak signal.

In this report we detail the design and fabrication of a new multi-material based SCAµTT platform compatible with fluorescent imaging. The platform takes advantage of IP-Visio, a new photoresin developed by Nanoscribe with reduced autofluorescence, and IP-S, which was found to have superior mechanical properties and produce more stable platforms than IP-Visio alone. In addition, we incorporated integrated apertures made by evaporating gold on to the substrate to prevent the illumination of IP-S, further reducing background noise and improving signal-to-noise ratio during imaging. With this design, we demonstrated the ability to image F-actin and the nucleus in a pair of keratinocytes as they are stretched up to 250% strain, allowing us to observe junction rupture and F-actin retraction while simultaneously recording the accumulation of over 800 kPa of stress in the junction. The platform presented here will enable potential studies on mechanotransduction at the cell-cell junction by monitoring fluorescently tagged proteins and tension levels in mechanosensitive networks using FRET,

and the fabrication technique can be integrated into other TPP-printed platforms for use in cell mechanics studies.

2 Materials and methods

2.1 TPP fabrication

TPP processing was carried out using a Photonic Professional GT (Nanoscribe GmbH) instrument and two proprietary photoresins, IP-S and IP-Visio, supplied by the vendor. The 3D computer assisted designs (CAD) of SCAµTT platforms were compiled using the 3D graphic editor built into COMSOL Multiphysics software. Subsequently, STL files of 3D CAD designs were exported and converted into job files using DeScribe software. When printing IP-S parts of SCAµTT platforms, the laser beam scanning velocity and laser power were set to 55 mm/s and 65%, respectively. The interlayer and raster distances (commonly referred to as "slicing" and "hatching" distances, respectively) were set to be 0.5μ m and 0.4μ m. For printing IP-Visio parts, scanning velocity, laser power, slicing distance, and hatching distance were 30 mm/s, 90%, 0.4 m, and 0.3 mm, respectively. These small slicing and hatching distances provide sufficiently high resolution and surface smoothness while printing time was reasonably short (a 6×6 array of these platforms can be fabricated overnight within 10–12 h). After printing arrays of the main parts of SCAµTT platforms, the substrates were successively soaked in SU-8 developer for 30 min, rinsed with isopropanol, dried, and loaded into the TPP tool. Similar development and drying procedures were used after printing the top IP-Visio platforms. Before printing the top IP-Visio platforms, alignment of the substrate with already printed IP-S structures was done manually by centering each IP-S structure in the field of view of the tool's optical camera. All IP-S and IP-Visio parts were fabricated using the solid mode.

To fabricate the apertures, sacrificial shadow masks were 3D printed on the substrates using the same tool used for printing SCAµTT platforms (See Fig. 4 for detailed illustration). The sacrificial shadow masks were elevated disks supported by four tapered pillars and sized according to the targeted aperture diameter. The size and tapered shape of the pillars supporting the disks were selected based on preliminary tests in which arrays of such structures were printed with various sizes of supporting elements and subjected to a gentle stream of deionized (DI) water from a typical showerhead used for sample rinsing in a cleanroom setting. The sizes of the supporting pillars in the structures removed completely by the water stream were selected and subsequently used in this study. Arrays of sacrificial disk structures with the previously identified sizes of supporting pillars were printed on cover slips and subsequently coated



with a stack of 50 nm gold (Au) on 10 nm titanium (Ti) using a Thermionics VE-420 dual source e-gun evaporator (Thermionic Inc.). Once the metallization was completed the printed sacrificial disk arrays were removed with a gentle stream of DI water from a showerhead leaving only the metal with apertures patterned on the substrates.

The deposition of the nanoporous silicon oxide layer was done using near-room temperature plasma-enhanced chemical vapor deposition (PECVD) on an Oxford Plasmalab System 100 (Oxford Instruments Inc.) tool in a mixture of silane (SiH₄), argon (Ar), and nitrous oxide (N₂0). The procedure was described previously (Charlton et al. 2014). In brief, the main parameters of the PECVD recipe were as follows: 25–30 °C substrate temperature, 600 mTorr pressure, and 150-W RF power. Flow rates of 5% SiH₄ in Ar and N₂0 were 75 cm³ min⁻¹ and 600 cm³ min⁻¹, respectively. Deposition rate was approximately 100 nm per minute. From here fabrication of the SCA μ TT platforms was carried out as described above.

2.2 Cell culture and staining

A431 cells were cultured in Dulbecco's modified Eagle's medium (DMEM) (Thermo Fisher) supplemented with 10% fetal bovine serum (FBS) (Thermo Fisher) and 1% penicillin–streptomycin (P/S) (Thermo Fisher). Keratinocyte cells (HaCaT) were cultured in DMEM with low calcium concentration (Thermo Fisher) and supplemented with 10% FBS, 1% P/S, and 1% GlutaMAX (Thermo Fisher). For experiments, cells were grown in $\rm CO_2$ independent DMEM (Thermo Fisher) supplemented with 10% FBS and 1% P/S.

A431 cells were first fixed with 4% paraformaldehyde diluted from 16% paraformaldehyde (Thermo Fisher) in phosphate-buffered saline (PBS) (Thermo Fisher) for 10 min. Then, cells were permeabilized with 0.1% Triton X-100 (Sigma-Aldrich) for 5 min. To stain zyxin, anti-zyxin antibody (Sigma) was diluted to a ratio of 1:250 v/v in PBS, added to the sample, refrigerated for 24 h, and finally washed twice with PBS. Then, goat anti-rabbit IgG(H + L), Superclonal Recombinant Secondary Antibody, Alexa Fluor 647 (Thermo Fisher) was incubated with the sample for 1 h at 37 °C. To stain F-actin, Alexa Fluor 488 Phalloidin (Invitrogen) was diluted to a 1X concentration in PBS and incubated in the sample at room temperature for 30 min. Finally, to stain the nucleus, DAPI (Thermo Fisher) was diluted 1:1000 in PBS and incubated with the sample for 10 min at room temperature and then filled with PBS for imaging. Between each of the above steps, the sample was washed twice with PBS. HaCaT cells were fixed, permeabilized, and stained for F-actin and the nucleus with the same parameters as A431 cells. Between each step, cells were washed two times by incubating in PBS at room temperature for 4 min. These staining protocols were kept the same for each sample under different comparison groups in the same study.

2.3 Cell deposition and stretching

Prior to cell deposition, SCAµTT platform arrays were placed in a glass bottom petri dish and sterilized with 70% ethanol for 1 min and then soaked in PBS for 1 h to dissolve any remaining ethanol. Then, the platforms were coated with Geltrex (Thermo Fisher) for 1 h to promote adhesion of cells onto the platform. In preparation for cell deposition, 2 mL of CO₂-independent DMEM was placed in the petri dish. After cells were passaged, 100 µL of cells suspended in DMEM at a concentration of 500 cells/µL was dropped on top of the platforms. For depositing cells on the platforms, an Eppendorf single-cell isolation setup was used. The setup consists of a pressure controller (Cell-Tram 4r Air/Oil, Eppendorf) which controls the pressure inside a microcapillary (Piezo Drill Tip ICSI, Eppendorf) with a tip inner diameter of 6 µm. The pressure controller is positioned with a 3D manipulator (TransferMan 4r, Eppendorf), which is on a Nikon Eclipse Ti-S microscope within a temperature-controlled chamber at 37 °C. To deposit cells, the tip of the microcapillary is brought into contact with a cell on the substrate. Subsequently, a negative pressure is applied to suction the cell to the tip. The cell is brought into one side of the bowtie confinement on top of the SCAµTT platform and the pressure is released to place the cell. The same procedure is then repeated to place another cell on the other side of the confinement, and this process is repeated for each platform in the array.

The cell stretching setup consists of an AFM (Nanosurf AG, Switzerland) on a Zeiss Axio Observer 7 microscope. A hole is drilled in the tip of the AFM probe with focused ion beam (FIB) etching in a FEI Helios NanoLab 660. For stretching cells on the hybrid design, first the islands are separated by breaking the tethers that join the islands, which were implemented to promote stability of the structures, using the microneedle tip used for cell deposition. The sample is placed under the AFM and the AFM tip with a through hole is lowered to the device to capture the pin on the forcing island. The cell pair was stretched in increments of 5 μ m by moving the AFM tip with the AFM software and imaged at each point from 0 μ m to 50 μ m (with a time of about 22 s between each image).

2.4 Signal quantification

To quantify the signal intensity from images of disks in the initial comparison of autofluorescence between IP-S and IP-Visio, a circular region of interest was drawn on each disk and the intensity for each channel was calculated with Zeiss software. An average of these values for all disks was then calculated. For quantifying the intensity



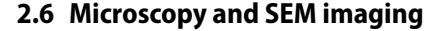
of stains of zyxin, F-actin, and DAPI, small regions of interest were defined in areas with high signal with well-defined features of the proteins, and the average intensity of these regions of interest was calculated.

To quantify the signal intensity from images of the original SCA μ TT platform as well as the hybrid SCA μ TT platform without and with integrated apertures, a small rectangular region of interest (Fig. 5a) was defined within the bowtie confinement area of each device imaged, and the average intensity within the region of interest was calculated with Zeiss software. Then, the average of each of these values for the same type of platform was calculated.

To quantify the intensity of stained nuclei on the platforms, a custom CellProfiler (Broad Institute) pipeline was created to identify the nuclei and calculate their average intensity. To calculate the background signal for each nucleus, images of the platforms without stained cells were taken with the same image acquisition parameters. Then, based on the border of each nuclei identified by CellProfiler, the intensity within the regions that the nuclei contain were calculated. The intensity of an individual nucleus is then calculated by subtracting this value from the original intensity, which would include signal from both the nucleus and background. To calculate signal-tonoise ratio, this value was divided by the background value for each nucleus, and then these values were averaged. To calculate the adjusted nucleus intensity, which takes into account the potential for variability of staining between samples, the average nucleus intensity in cells growing on the petri dish within which the platforms are placed was calculated, and the nucleus intensity of cells on the platform was divided by this value. This allows us to gauge accurately the effect SCAµTT platforms have on inhibiting signal excitation and collection.

2.5 Stress-strain curve calculation

The top plate displacement was assumed to match the input displacement and used to find the relationship between pixels and distance in μm . The bottom plate displacement was found by tracking bright spots on the edge of the bowtie with a MATLAB code. To convert bottom plate displacement to force, the stiffness of the vertical beams of the bottom island was calculated based on its dimensions and the dimensions and stiffness of the vertical beams of the original platform. The effective stiffness of the vertical beams supporting the sensing island in the original design was 0.11 N/m. Based on beam bending theory, the stiffness of the beams of the hybrid design with a height of 125 μm and thickness of 10 μm was calculated to be 49.2 N/m. From here, stress and strain were calculated as described previously (Esfahani et al. 2021).



Imaging was done on a Zeiss LSM800 Confocal laser scanning microscope and a Zeiss Axio Observer 7 microscope. Images for the initial comparison of autofluorescence between IP-S and IP-Visio were done on the confocal microscope, and all other images were taken on the Observer 7 unless specified otherwise. Imaging parameters such as laser power, master gain, and objective pinhole diameter were kept consistent between experiments to ensure consistency. Scanning electron microscope (SEM) images were taken on a FEI Helios NanoLab 660 SEM.

2.7 Mechanical characterization

To calculate the Young's modulus of IP-S and IP-Visio, a Hysitron TI 950 Triboindenter was used to indent bulk disks of IP-S and IP-Visio. First, the reduced modulus E_r was calculated through the indention experiment for each material. The Young's modulus was then calculated based on the following equation: $E = E_r(1 - v^2)$, assuming v = 0.4. Tensile tests were done by repurposing the original design of the SCAµTT platform for stretching crosslinked microfibers of IP-S and IP-Visio. The islands of these platforms were connected by crosslinking a microfiber of either IP-S or IP-Visio between them. Stretching was done with an AFM, and stress and strain information were obtained using digital image correlation. The Young's modulus was calculated by fitting the linear portion of the resulting stress-strain curves, and yield strength was determined as the intersection of the stress-strain curve with a 2% parallel offset line.

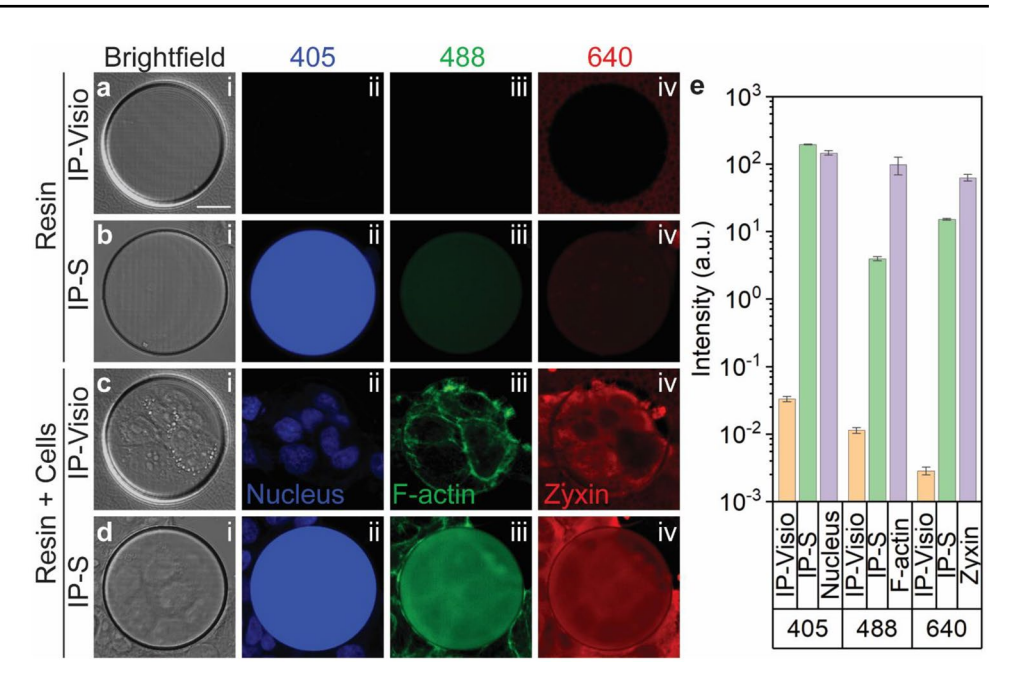
3 Results

3.1 Fluorescent properties of IP-S and IP-Visio

As a first test to gauge the fluorescent properties of IP-Visio, disks were fabricated from IP-S and IP-Visio and imaged with laser wavelengths of 405 nm, 488 nm, and 640 nm to measure their fluorescence across a range of possible imaging wavelengths. As shown in Fig. 1a and b, compared with IP-S, IP-Visio produces far less fluorescence in all channels. Next, A431 cells were cultured on the disks and stained for the nucleus, F-actin, and zyxin. As a result of the lower autofluorescence of IP-Visio compared to IP-S, more signal and details in the stains can be observed (Fig. 1c and d). The difference is most distinct in the 405 nm channel, in which the nucleus of individual cells can be clearly seen on IP-Visio but are completely blocked when imaged on IP-S due to its high autofluorescence in this channel (Fig. 1c and d, ii). In the 488 nm channel, more defined features of F-actin around the cell-cell junctions can be seen on IP-Visio, whereas these



Fig. 1 Fluorescent properties of IP-S and IP-Visio. For each image set: brightfield image (i) and fluorescent image with 405 nm laser (ii), 488 nm laser (iii), and 640 nm laser (iv), **a**, **b**. IP-Visio disk (a) and IP-S disk (b) imaged under brightfield and fluorescent channels. c, d. A431 cells stained for nucleus. F-actin, and zyxin and imaged on top of IP-Visio (c) and IP-S (d) disks. e. Average intensity of IP-Visio and IP-S disks with no cells and average intensity of the selected stains for the respective channel of cells off disks (n = 9 for all conditions). Scale Bar: 20 µm (a)



features are blurred when imaged on IP-S (Fig. 1c and d, iii). Zyxin stained in the 640 nm channel follows a similar trend, in which more details can be seen on IP-Visio and are blurred on IP-S (Fig. 1c and d, iv). To quantitatively evaluate and compare the fluorescence of IP-S and IP-Visio, the average intensity of the disks in each channel were calculated, along with the average intensity of prominent features of the nucleus, F-actin, and zyxin in A431 cells stained on a petri dish to compare these signals to autofluorescence produced by the TPP materials. As shown in Fig. 1e, the fluorescence of IP-S is many orders of magnitude greater than IP-Visio in the three channels tested, and additionally is within an order of magnitude of the fluorescence of the stains selected. These results demonstrate the potential of

IP-Visio as a material component to be used in fluorescent imaging of cells on the SCAμTT platform.

3.2 Fabrication of SCAµTT platform with IP-Visio

After demonstrating the potential of IP-Visio for use in fluorescent imaging of cells, we next sought to fabricate our SCAµTT platform with this material. As shown in Fig. 2a, the platform features two moveable islands supported by vertical beams of known stiffness, on which two cells are placed within the bowtie confinement area on each island. After cells adhere to the islands and form a mutual junction, the actuation island is displaced with an AFM probe, stretching the cells and deflecting the sensing island, the displacement

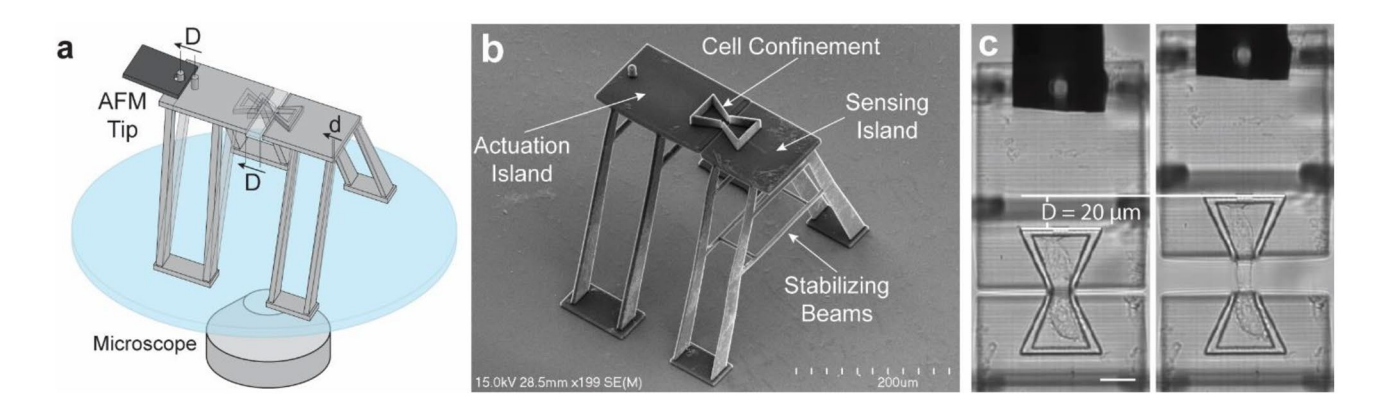


Fig. 2 Design of SCA μ TT platform. **a.** Working mechanism of SCA μ TT platform. Two cells are placed inside the cell confinement region that form a cell-cell junction across the gap between the islands. An AFM tip is used to displace the top island, and the bot-

tom island is bent under the force in the junction. **b.** SEM image of SCAμTT platform fabricated with IP-S. **c.** Brightfield image of a pair of A431 cells stretched to 20 μm. Scale Bar: 20 μm (**c**)



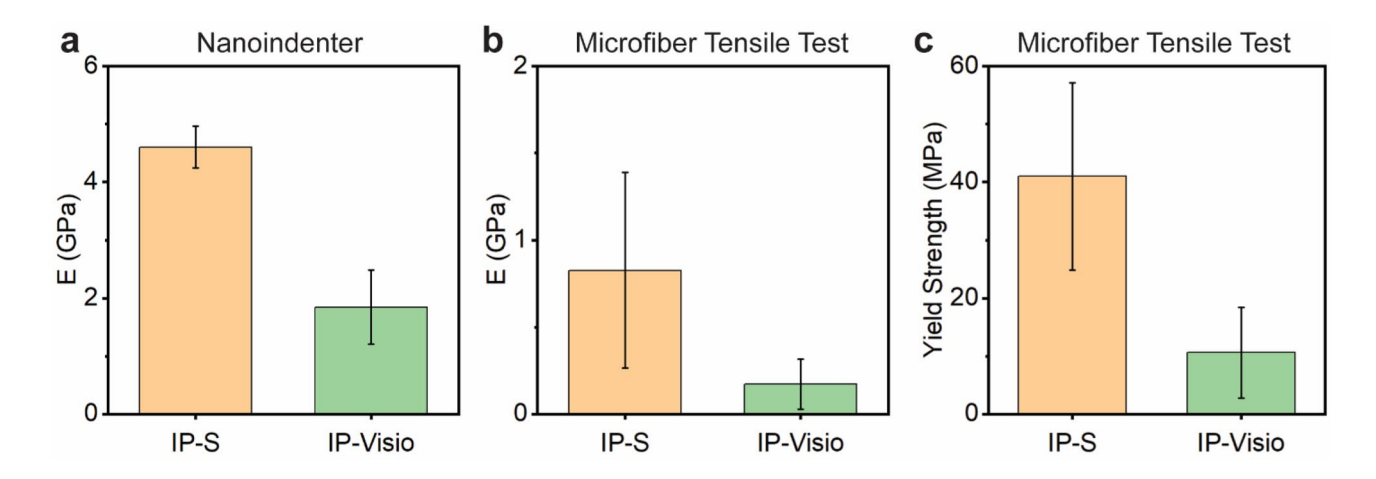


Fig. 3 Mechanical properties of IP-S and IP-Visio. **a**, **b**. Young's modulus of crosslinked IP-S and IP-Visio determined with nanoindentation (**a**) and in a microfiber tensile test (**b**). **c**. Yield strength of

crosslinked IP-S and IP-Visio determined in a microfiber tensile test. n=12 for both materials in nanoindentation test, and n=224 for IP-Visio and n=73 for IP-S in microfiber tensile test

of which is tracked to determine junctional stress based on the stiffness of the vertical beams. An SEM image of the platform fabricated with IP-S is shown in Fig. 2b, which is stable and dimensionally accurate with the nominal design. This platform can be used for stretching experiments, such as stretching a pair of A431 cells to 20 µm to observe failure mechanics of the junction (Fig. 2c). However, when fabricated with IP-Visio, the thin vertical beams collapse after fabrication. We next sought to characterize the mechanical properties of IP-S and IP-Visio to understand this behavior. Using nanoindentation, the Young's modulus of IP-S and IP-Visio were found to be 4.6 ± 0.75 GPa and 1.8 ± 0.64 GPa, respectively (Fig. 3a). Further, in a microfiber tensile test, the Young's modulus of IP-S and IP-Visio were found to be 0.83 ± 0.56 GPa and 0.17 ± 0.15 GPa, respectively (Fig. 3b). Despite the difference in magnitude from these quantification methods, this demonstrates that IP-Visio is weaker than IP-S. Further, using the microfiber tensile testing method, the yield strength of IP-S and IP-Visio were found to be 41 ± 16 MPa and 11 ± 7.8 MPa, respectively, further showing the superior strength of IP-S (Fig. 3c). In addition, we observed that IP-Visio parts tend to shrink significantly after development, leading to dimensional inaccuracies and making it an unideal candidate for fabricating the platform.

3.3 Fabrication of hybrid SCAµTT platform and integrated apertures

To produce a stable platform that can be used in experiments, a new design of our SCAµTT platform that incorporates both IP-S and IP-Visio was made. The design uses IP-S for the vertical beams due to its superior strength and crosslink stability, and IP-Visio for the top island where cells

are cultured and grow to allow for imaging with reduced background from autofluorescence. In this two-stage fabrication process shown in Fig. 4a, IP-S resin is cast on a glass slide coated in a porous silicon oxide layer and is crosslinked to yield the vertical beams. After developing, IP-Visio resin is cast on the slide and crosslinked to yield the islands with bowtie confinements. In the first attempts at fabricating this design, the islands would bend away from each other after fabrication, making it impossible for cells to form a junction with each other. To prevent this, IP-Visio links were added between the islands and the thickness of the vertical beams was increased. With these changes, a gap size between the islands that allows cells to form a junction with each other could be maintained, as revealed in an SEM image shown in Fig. 4b. In addition, the islands can easily be separated by breaking the IP-Visio tethers using the same deposition microneedle used to place cells on the device.

After preliminary images showed that the illumination of IP-S beams still caused increased background signal projected onto the cell confinement area, we developed a fabrication procedure to integrate apertures made with a gold coating into the porous silicon oxide layer, which can block illumination of the IP-S component. The fabrication procedure is shown in Fig. 4c, which begins with crosslinking an elevated disk of IP-S with a diameter matching the desired aperture diameter onto the glass slide before adding the porous silicon oxide layer. Next, a layer of gold is evaporated on the glass slide. As the porous silicon oxide layer helps promote adhesion between TPP printed parts and the glass slide, in its absence the disks can be easily washed off, leaving behind a pinhole in the gold coating layer through which light can pass. After adding the porous silicon oxide layer, the hybrid device can be fabricated as normal after carefully aligning the apertures on the substrate with the



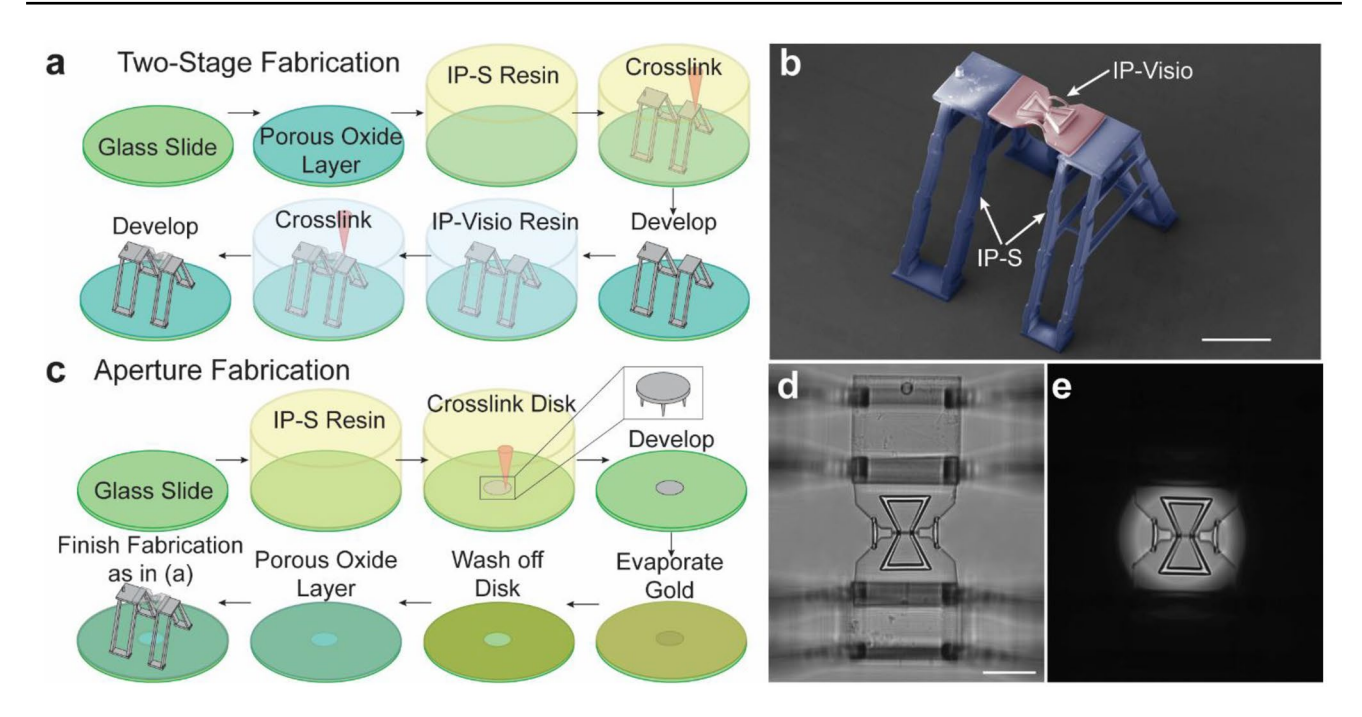


Fig. 4 Fabrication of hybrid tensile tester and integrated apertures. **a.** Two-stage fabrication of hybrid $SCA\mu TT$ platform, in which IP-S vertical beams are crosslinked first, followed by IP-Visio plates. **b.** SEM image of hybrid $SCA\mu TT$ platform (IP-S colored in blue, IP-

Visio colored in red). **c**. Fabrication of apertures integrated into the glass slide. **d**, **e** Brightfield image of hybrid SCA μ TT platform without (**d**) and with (**e**) an integrated aperture. Scale Bars: 100 μ m (**b**), 50 μ m (**d**)

TPP instrument. A brightfield image of this device without and with the integrated aperture demonstrates how light can pass through the aperture to illuminate the bowtie confinement fabricated from IP-Visio, while casting a shadow on the vertical IP-S beams (Fig. 4d and e).

3.4 Evaluation of background signal suppression

To compare the suppression of background signal generated by autofluorescence with these two new designs and the original design fabricated from IP-S, each platform was imaged and the background signal inside of the bowtie confinement, where cells would be during an experiment, was measured with different input laser wavelengths. For instance, for the 488 nm channel, the original design fabricated with IP-S has a much higher background signal compared to the hybrid design both without and with an optical blocking aperture (Fig. 5a-f). Quantifying the background intensity within the bowtie confinement shows that, while the background is suppressed in the hybrid design, it is almost two orders of magnitude smaller with the addition of the optical blocking aperture (Fig. 5g). To further understand the degree to which the integrated apertures can suppress background signal, we compared the background signal within the hybrid design without and with integrated apertures to background signal quantified in an image captured without the SCAµTT platform in the field of view (same Z-height, but different XY location), which would not be influenced by autofluorescence from IP-S or IP-Visio and can be considered the absolute background noise from image collection. We found that background signal on the hybrid platform without an integrated aperture is an order of magnitude greater than background far away from the SCA μ TT platform, but when an integrated aperture is used, the background signal is almost identical to background far away from the SCA μ TT platform (Fig. 5h). This demonstrates that the integrated apertures can almost completely suppress background signal generated by the SCA μ TT platform.

3.5 Signal collection and stretching of stained keratinocyte cells

While the optical blocking apertures can suppress background signal produced by the platform, it is important to consider their effect on exciting and collecting signal from cells on the device. Based on the objective and immersion liquid used in imaging, there is a cone of light defined by an angle α within which signal can be collected by the objective. Based on the height of the stretcher and aperture diameter, there is another cone of light defined by an angle β produced by signal from the cells that can be seen from underneath. If β is larger than α , signal collection is not impacted (Fig. 6a, i), but if β is smaller than α , then signal will be blocked (Fig. 6a, ii). To study the effect of the apertures blocking



33 Page 8 of 12 Biomedical Microdevices (2022) 24: 33

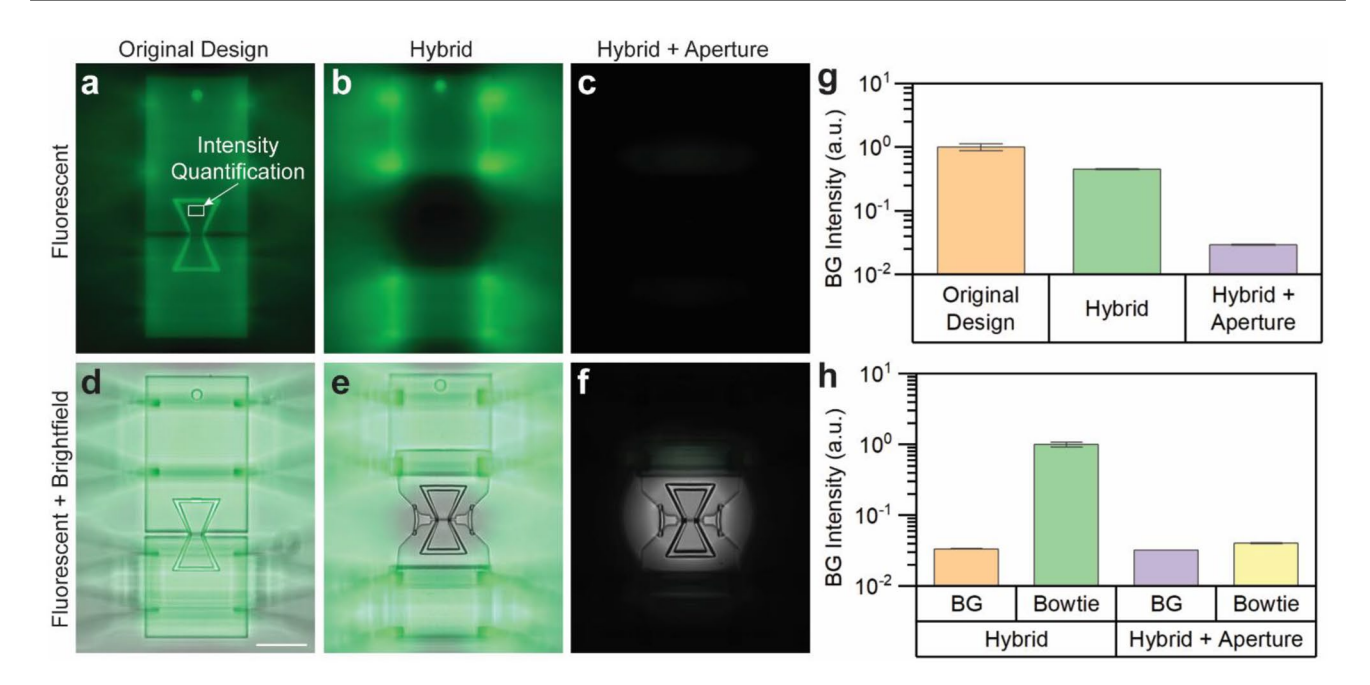


Fig. 5 Background noise is reduced in hybrid SCA μ TT platform. **a**-**c** Fluorescent image of SCA μ TT platform fabricated from IP-S (**a**) and hybrid SCA μ TT platform without (**b**) and with (**c**) integrated apertures. **d-f** Fluorescent and brightfield image overlay of the same three platforms. **g.** Average background (BG) intensity of the three platforms within the bowtie confining region (n = 10 for original

design and hybrid, n=42 for hybrid + aperture). **h**. Average background intensity within bowtie confining region of the hybrid platform without and with integrated apertures compared to background signal obtained from images with no SCA μ TT platforms (n=3 for all conditions, aperture diameter and platform height are 120 μ m and 80 μ m, respectively, for hybrid + aperture). Scale Bar: 50 μ m (**d**)

signal from cells on the platform, HaCaT cells were deposited on platforms with various combinations of vertical beam height and aperture diameter, as well as platforms with no optical blocking aperture, and stained for their nucleus and F-actin. After imaging, the average intensity of each nucleus was quantified and compared with background signal generated by the platform in the same spot as the nucleus. The intensity of each nucleus was divided by the average nucleus intensity of cells on the petri dish far away from the platform to account for variability in staining efficiency between samples. By comparing this adjusted nucleus intensity to the angle β formed by the platform height and aperture diameter, the signal collected was found to linearly increase for angles below 45 degrees. However, the intensity of nuclei on the device with no apertures, which have an effective angle of 90 degrees, does not follow this trend and is less than the intensity expected based on the linear trend (Fig. 6b). Similarly, the signal-to-noise ratio, calculated as the adjusted nucleus intensity divided by the background signal, can be seen to increase as the angle increases up to 45 degrees, but does not increase linearly and instead curves down (Fig. 6c). At an angle of 90 degrees, the signal-to-noise ratio decreases to a similar level as an angle of around 15 degrees.

Representative images of cells on the original platform, the hybrid design with no aperture (90 degrees), and the hybrid design with a small angle (14.5 degrees) and an

intermediate angle (36.9 degrees) are shown in Fig. 6d-f. The images are scaled to have the same nucleus intensity in each image to see the clarity of the images. For a standard fluorescent microscope, images on the original design fabricated from IP-S have a high level of autofluorescence, obscuring details in the images of the cells (Fig. 6d-f, i). The hybrid platform with no aperture allows for these details to be seen, but increased background noise from illumination of IP-S still obscures some details and results in a low signal-to-noise ratio (Fig. 6d-f, ii). The images on platforms with a low angle can be seen to have a low signal-to-noise ratio, due to the aperture blocking either the excitation or collection of signals from the cells (Fig. 6d-f, iii). For an intermediate angle, noise produced from IP-S is blocked while not compromising signal stimulation and collection, resulting in a high signal-to-noise ratio (Fig. 6d-f, iv). When imaged on a confocal microscope, images taken on the hybrid platform appear to have a similar signal-tonoise ratio between the three platforms with a slight loss of signal from the platform with a small angle. This is due to the image acquisition being done pixel-by-pixel on a confocal microscope, therefore minimizing the effect illuminating surrounding IP-S has on increasing background noise within the confinement area (Fig. 6f).

We finally demonstrated the utility of the device by stretching a pair of HaCaT cells on the hybrid platform



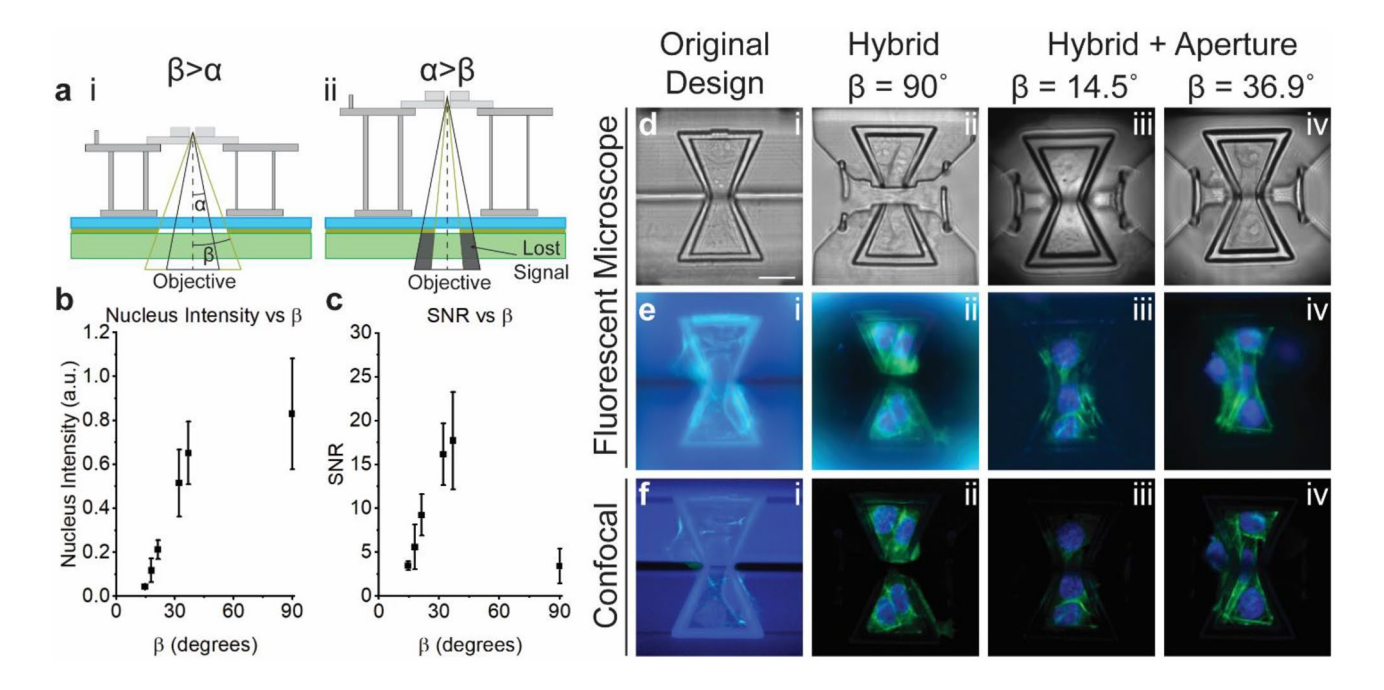


Fig. 6 Integrated apertures can increase signal-to-noise ratio without inhibiting signal stimulation and collection. **a**. The half-angles α and β are determined by the optics of the image collection system and the dimensions of the height of the platform and the diameter of the aperture, respectively. When $\beta > \alpha$, signal is not lost (i). When $\alpha > \beta$, signal is lost (ii). **b**, **c**. Average intensity (**b**) and signal-to-noise ratio (SNR) (**c**) of nuclei imaged on SCAμTT platforms with varying values of β , with no aperture representing 90° (n = 8–15 for conditions

with aperture, and n=44 for condition with no aperture). **d-f.** Representative images of cells stained on the original SCA μ TT platform (i), the hybrid design with no aperture (ii), and the hybrid design with apertures with a small angle which restricts signal collection (iii) and a large angle with minimal interference on signal collection (iv). Images were captured on a standard fluorescent microscope (**d-e**) and a confocal microscope (**f**). Scale Bar: 20 μ m (**d**)

with an optical blocking aperture with an angle β of 17.9 degrees. After the cells were stained, the IP-Visio links were broken using the deposition microneedle to disconnect the islands and allow for stretching of the stained pair of cells. The cells were stretched in increments of 5 μ m and imaged for the nucleus and F-actin (Fig. 7a). The displacement of the bottom island was determined by tracking the location of the edge of the bowtie confinement in each image

(Esfahani et al. 2021). Despite having a low angle which can block signal, the suppression of background noise still allows for visualizing the nucleus and cytoskeleton from the stains. From the images, it can be seen that the cell pair is stretched to a strain of 91% without damage, and signs of damage to the cell pair begin around a strain of 140%. When the maximum strain of 244% is reached, the cell junction fully ruptures. From displacement data and the stiffness of

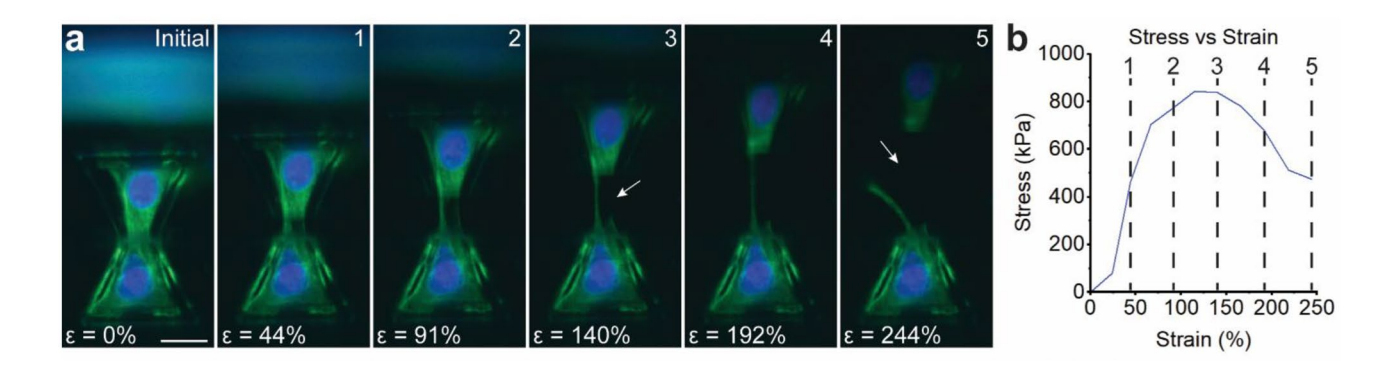


Fig. 7 Hybrid SCA μ TT platform with integrated aperture allows for stretching and imaging a pair of HaCaT cells. **a**. A pair of HaCaT cells stained for F-actin and nucleus and stretched to 50 μ m. **b**. Corre-

sponding stress-strain curve for stretched cell pair in (a), with points labeled that correspond to images in (a). Scale Bar: $20 \mu m$ (a)



the sensing island vertical beams, a stress-strain curve for this cell pair is produced (Fig. 7b). Stress in the junction increases to over 800 kPa, at which point fracture in the junction is initiated. As the cell pair is stretched further, the stress in the junction decreases until it finally ruptures. It should be noted that this peak value of stress was much higher than our previously reported values (Esfahani et al. 2021). This could be explained by the differences in cell type as well as stretching fixed cells in this study, which have been found have a Young's modulus nearly five times larger than living cells (Kim et al. 2017).

4 Discussion

We report the design, fabrication, and testing of a novel TPP-printed platform for investigating mechanotransduction in a single cell-cell junction. The fluorescent properties of IP-Visio, a new proprietary photoresist from Nanoscribe, were investigated and compared with IP-S, a photoresist from Nanoscribe that has been used extensively in TPP fabrication. Compared with IP-S, IP-Visio was found to be significantly less autoflourescent across a spectrum of tested excitation wavelengths and staining of cells on top of IP-S and IP-Visio showed the potential of exciting and collecting signal from cells on IP-Visio. However, mechanical characterization of the two materials showed that IP-Visio has a significantly lower Young's modulus and yield strength compared to IP-S; therefore, it may not be suitable for making the flexible components and for force sensing, such as the vertical beams in our SCAµTT platform.

To address this shortcoming, we designed a new hybrid multi-material based SCAµTT platform that uses IP-S for the thin vertical beams for actuation and sensing and IP-Visio for part of the islands on which cells are cultured and imaged. To further combat increased background that resulted from illumination of IP-S during imaging, we developed a fabrication approach for integrating optical apertures with a gold coating on the glass slide on which SCAμTT platforms are printed. Our results showed that, compared to the original SCAµTT platform fabricated with IP-S, the hybrid design produces significantly lower background signal within the cell confinement region, and the integrated apertures further reduce background. Next, considering the potential of the integrated apertures to interfere with the excitation and collection of signals from cells, we quantified the intensity of cell nuclei stained on platforms with varying combinations of aperture diameter and height. We found that combinations of these parameters that produced a small characteristic angle β resulted in reduced signal excitation and collection with a low signal-to-noise ratio, compared to platforms with no coating which have a low signal-to-noise ratio due to illumination of IP-S increasing background signal. More importantly, we showed that platforms with intermediate angles allow for excitation and collection of almost all signal from cells on the platform while increasing signal-to-noise ratio by blocking the illumination of IP-S. Finally, we demonstrated the potential of the platform for imaging a single cell pair as they were stretched while simultaneously recording stress and strain in the junction. Keratinocyte cells were stretched to almost 250% strain with a peak stress over 800 kPa. Imaging of F-actin allowed for direct visualization of the cytoskeleton being deformed and the junction rupturing, which was initiated around a strain of 140% before the peak junction stress was observed.

In other studies that use TPP platforms for mechanobiology, a variety of approaches have been used to either limit fluorescence of the TPP materials or to mitigate the effects of illuminating TPP materials on signal-to-noise ratio. To limit fluorescence of TPP materials, nonfluorescent dyes such as sudan black (Flamourakis et al. 2021; Jaafar et al. 2011; Qi et al. 2017; Maggi et al. 2017) have been used to quench autofluorescence in all channels, and dyes can potentially be incorporated to induce high fluorescence in a specific channel and reduce autofluorescence in other channels. While this approach can reduce autofluorescence, these additives can be non-biocompatible and even toxic to cells. In addition, as the photoinitiator used for crosslinking in TPP is a significant contributor to autofluorescence, another approach is to use photoinitiators with lower autofluorescence in TPP printing (Raimondi et al. 2014). However, this can result in a variety of changes to the physical or chemical properties of the resulting device; therefore, this is not always an option. In addition, prolonged illumination of printed materials can reduce their autofluorescence, and can be used as a pretreatment step (Piruska et al. 2005). However, this method cannot eliminate autofluorescence, and some autofluorescence recovers after a period of time and is therefore not compatible for applications where cells are cultured for many hours. To avoid autofluorescence, infrared fluorophores can be used, as TPP materials generally have lower autofluorescence at the excitation wavelength of these fluorophores (Hong et al. 2017). However, microscopes equipped with the appropriate filters and detectors for imaging these fluorophores are not common. In addition, image processing techniques can be used to estimate autofluorescence by imaging at a slightly different excitation wavelength and subtracting it from the image (Tanhuanpää et al. 2000). However, this assumes that autofluorescence will be the same across different wavelengths, which is not always true, and additionally requires extra images to be collected, lowering the image acquisition rate. Another approach is to use microscopes with different methods of image acquisition that mitigate the autofluorescence of TPP materials. For example, in two-photon imaging, infrared light is focused on the sample, where fluorescence is



induced by the simultaneous absorption of two photons in a fluorophore. Infra-red light can pass through materials more easily compared to visible light, which limits exposure of these materials and mitigates autofluorescence (Accardo et al. 2017; Svoboda and Yasuda 2006). In addition, as we showed here (Fig. 6f), a confocal microscope, which creates images by scanning and capturing signal pixel-by-pixel, can avoid illumination of highly autofluorescent materials surrounding cells during stimulation and capturing of signal, reducing background noise. Despite these capabilities, it is less common for researchers to have access to these types of microscopes, and if they do, they are usually expensive to use.

The platform designed in this report, as well as the ideas and techniques used in its design, can be used for fluorescent imaging of cells on TPP platforms with standard fluorescent microscopes. The hybrid SCAµTT platform can be used to study mechanotransduction processes mediated by stress and strain accumulation in cell-cell junction expressing FRET molecules, which will be the focus of our next study. Signal from FRET molecules is inherently weak, and the high signal-to-noise ratio of our SCAµTT platform with integrated apertures has potential to allow for the stimulation and capturing of this signal while the cell-cell junction is mechanically stimulated. For example, mechanosensitive proteins within cell-cell junctions can be probed to study the transmission of forces in the junction. Forces has been shown to be transmitted through desmosomes and adherens junctions using FRET sensors in desmoplakin (Price et al. 2018) and E-cadherin (Borghi et al. 2012), respectively, under externally applied stretch, and the hybrid SCAµTT platform can be used to further investigate how forces within these individual junctions relate to stress within the entire cell-cell contact. In addition, FRET sensors have been integrated into mechanosensors such as α-catenin (Kim et al. 2015) to study conformation changes that expose a cryptic binding site for vinculin, and our platform can be used to investigate the levels of stress in the cell-cell junction that are required for its activation. In addition, the platform can be used for studying phenomena such as force-induced clustering of E-cadherin in the cell-cell junction under applied stress using cells expressing fluorescently tagged E-cadherin, which has been theorized to occur based on simulation studies of E-cadherin dynamics (Chen et al. 2021; Thompson et al. 2020; Yu et al. 2022). Further, remodeling of the cytoskeleton has been observed in response to applied forces, such as force across VE-cadherin inducing F-actin polymerization (Barry et al. 2015), and can be investigated further on our platform using cells expressing fluorescent tags on cytoskeleton proteins such as F-actin or intermediate filaments. Finally, as the platform allows time for the formation of mature focal adhesions, the transmission of force from the cell-cell junction to cell-ECM junctions can be studied with a variety of techniques, including FRET,

fluorescent tags, and cell-ECM force probes such as tension gauge tethers (Rao et al. 2020), DNA hairpin sensors (Li et al. 2021), and traction force microscopy (Broussard et al. 2017; Liu et al. 2010).

The approach detailed in this report of integrated apertures to block illumination of autofluorescent materials can also be used in other studies. For example, microfluidic devices are commonly fabricated from autofluorescent materials, such as SU-8, which can interfere with fluorescent imaging (Narayan et al. 2018; Pai et al. 2007; Walczak et al. 2011). Integrated apertures could be used in these devices to minimize unwanted fluorescence from the bulk material.

Despite these promising results, there remain some limitations to our approach. For instance, we have observed that the hybrid fabrication approach with IP-S and IP-Visio results in residual stress accumulation and dimensional inaccuracies of IP-S components. We hypothesize that these observations are the result of interaction between crosslinked IP-S and uncrosslinked IP-Visio resin during the two-stage fabrication. Residual stress could lead to inaccuracies in calculating the stress in the junction due to the small length scale at which the sensing island deforms under forces tolerated by the cell-cell junction and will be further investigated.

Acknowledgements We thank Dr. Benjamin Richter from Nanoscribe GmbH for the helpful discussions.

Funding We acknowledge the funding support from the NSF (Awards 1826135, 1936065, 2143997), the NIH National Institutes of General Medical Sciences P20GM113126 (Nebraska Center for Integrated Biomolecular Communication) and P30GM127200 (Nebraska Center for Nanomedicine), the Nebraska Collaborative Initiative and the Voelte-Keegan Bioengineering Support. Design and fabrication of the TPP structures were conducted at the Center for Nanophase Materials Sciences (CNMS) at ORNL, which is a DOE Office of Science User Facility. Manufacturing and characterization analysis were performed at the NanoEngineering Research Core Facility (NERCF). G.M. and J.R. are funded by the NSF Graduate Research Fellowship (Award 2034837).

Declarations

Competing interests The authors declare no competing interests.

References

- A. Accardo, M.-C. Blatché, R. Courson, I. Loubinoux, C. Thibault, L. Malaquin, C. Vieu, Small. 13, 1700621 (2017)
- A.K. Barry, N. Wang, D.E. Leckband, J. Cell. Sci. 128, 1341–1351 (2015)
- N. Borghi, M. Sorokina, O.G. Shcherbakova, W.I. Weis, B.L. Pruitt, W.J. Nelson, A.R. Dunn, Proc. Natl. Acad. Sci. 109, 12568–12573 (2012)
- J.A. Broussard, R. Yang, C. Huang, S.S.P. Nathamgari, A.M. Beese, L.M. Godsel, M.H. Hegazy, S. Lee, F. Zhou, N.J. Sniadecki, K.J. Green, H.D. Espinosa, Mol. Biol. Cell. 28, 3156–3164 (2017)



33 Page 12 of 12

- J.J. Charlton, N. Lavrik, J.A. Bradshaw, M.J. Sepaniak, ACS. Appl. Mater. Interface. 6, 17894–17901 (2014)
- Y. Chen, J. Brasch, O.J. Harrison, T.C. Bidone, Biophys. J. 120, 4944–4954 (2021)
- A.M. Esfahani, J. Rosenbohm, B.T. Safa, N.V. Lavrik, G. Minnick, Q. Zhou, F. Kong, X. Jin, E. Kim, Y. Liu, Proc. Natl. Acad. Sci. 118, e2019347118 (2021)
- G. Flamourakis, A. Kordas, G.D. Barmparis, A. Ranella, M. Farsari, Opt. Mater. Express. 11, 801–813 (2021)
- J. Friedrichs, K.R. Legate, R. Schubert, M. Bharadwaj, C. Werner, D.J. Müller, M. Benoit, Methods. 60, 169–178 (2013)
- B. González-Bermúdez, G.V. Guinea, G.R. Plaza, Biophys. J. 116, 587–594 (2019)
- G. Hong, A.L. Antaris, H. Dai, Nat. Biomed. Eng. 1, 1–22 (2017)
- I.H. Jaafar, C.E. LeBlon, M.-T. Wei, D. Ou-Yang, J.P. Coulter, S.S. Jedlicka, Acta. Biomater. 7, 1588–1598 (2011)
- S.-O. Kim, J. Kim, T. Okajima, N.-J. Cho, Nano. Converg. 4, 1–8 (2017)
- T.-J. Kim, S. Zheng, J. Sun, I. Muhamed, J. Wu, L. Lei, X. Kong, D.E. Leckband, Y. Wang, Curr. Biol. 25, 218–224 (2015)
- H. Li, C. Zhang, Y. Hu, P. Liu, F. Sun, W. Chen, X. Zhang, J. Ma, W. Wang, L. Wang, Nat. Cell. Biol. 23, 642–651 (2021)
- Z. Liu, J.L. Tan, D.M. Cohen, M.T. Yang, N.J. Sniadecki, S.A. Ruiz, C.M. Nelson, C.S. Chen, Proc. Natl. Acad. Sci. U. S. A. 107, 9944–9949 (2010)
- A. Maggi, H. Li, J.R. Greer, Acta. Biomater. 63, 294-305 (2017)
- S. Narayan, K. Bae, R. Lehn, S. Yadav, M. Ott, T. Meckel, R.W. Stark, J. Micromech. Microeng. 28, 125001 (2018)
- J.-H. Pai, Y. Wang, G. To'A Salazar, C.E. Sims, M. Bachman, G.P. Li, N.L. Allbritton, Anal. Chem. 79, 8774–8780 (2007)
- P. Panorchan, J.P. George, D. Wirtz, J. Mol. Biol. 358, 665–674 (2006)
 A. Piruska, I. Nikcevic, S.H. Lee, C. Ahn, W.R. Heineman, P.A. Limbach,
 C.J. Seliskar, Lab. Chip. 5, 1348–1354 (2005)

- A.J. Price, A.-L. Cost, H. Ungewiß, J. Waschke, A.R. Dunn, C. Grashoff, Nat. Commun. 9, 1–11 (2018)
- L. Qi, E.K. Knapton, X. Zhang, T. Zhang, C. Gu, Y. Zhao, Sci. Rep. 7, 1–12 (2017)
- M.T. Raimondi, M.M. Nava, S.M. Eaton, A. Bernasconi, K.C. Vishnubhatla, G. Cerullo, R. Osellame, Micromachines. 5, 341–358 (2014)
- T.C. Rao, V.P.-Y. Ma, A. Blanchard, T.M. Urner, S. Grandhi, K. Salaita, A.L. Mattheyses, J. Cell. Sci. 133, jcs238840 (2020)
- K. Svoboda, R. Yasuda, Neuron, **50**, 823–839 (2006)
- H. Tabdili, M. Langer, Q. Shi, Y.-C. Poh, N. Wang, D. Leckband, J. Cell Sci. 125, 4362–4371 (2012)
- K. Tanhuanpää, J. Virtanen, P. Somerharju, Biochim. Biophys. Acta. Mol. Cell. Res. 1497, 308–320 (2000)
- C.J. Thompson, Z. Su, V.H. Vu, Y. Wu, D.E. Leckband, D.K. Schwartz, Elife. 9, e59035 (2020)
- S.R.K. Vedula, T.S. Lim, P.J. Kausalya, E.B. Lane, G. Rajagopal, W. Hunziker, C.T. Lim, Exp. Mech. 49, 3–9 (2009)
- R. Walczak, P. Sniadek, J.A. Dziuban, Opt. Appl. 41, 873–884 (2011)
 Q. Yu, W.R. Holmes, J.P. Thiery, R.B. Luwor, V. Rajagopal, Biophys. J. 121, 596–606 (2022)

Publisher's Note Springer Nature remains neutral with regard to jurisdictional claims in published maps and institutional affiliations.

Springer Nature or its licensor holds exclusive rights to this article under a publishing agreement with the author(s) or other rightsholder(s); author self-archiving of the accepted manuscript version of this article is solely governed by the terms of such publishing agreement and applicable law.

